

## Downstream plasma transport and metal ionization in a high-powered pulsed-plasma magnetron

Liang Meng, He Yu, Matthew M. Szott, Jake T. McLain, and David N. Ruzic

Citation: [Journal of Applied Physics](#) **115**, 223301 (2014); doi: 10.1063/1.4878622

View online: <http://dx.doi.org/10.1063/1.4878622>

View Table of Contents: <http://scitation.aip.org/content/aip/journal/jap/115/22?ver=pdfcov>

Published by the [AIP Publishing](#)

---

### Articles you may be interested in

[Time-resolved investigation of dual high power impulse magnetron sputtering with closed magnetic field during deposition of Ti-Cu thin films](#)

[J. Appl. Phys.](#) **108**, 043305 (2010); 10.1063/1.3467001

[Design and characterization of 2.45 GHz electron cyclotron resonance plasma source with magnetron magnetic field configuration for high flux of hyperthermal neutral beam](#)

[Rev. Sci. Instrum.](#) **81**, 083301 (2010); 10.1063/1.3477998

[Sheath and potential characteristics in rf magnetron sputtering plasma](#)

[J. Appl. Phys.](#) **100**, 083303 (2006); 10.1063/1.2360384

[Effects of substrate bias on electron energy distribution in magnetron sputtering system](#)

[Phys. Plasmas](#) **11**, 4796 (2004); 10.1063/1.1786592

[Anomalous behaviors of plasma parameters in unbalanced direct-current magnetron discharge](#)

[Phys. Plasmas](#) **11**, 3595 (2004); 10.1063/1.1759629

---

A promotional banner for the 2014 Special Topics in AIP Materials. The banner has an orange background with a white border. At the top, the text '2014 Special Topics' is written in a large, white, sans-serif font. Below this, there are five circular icons, each containing a different material structure and a label: 'PEROVSKITES' (red and black geometric shapes), '2D MATERIALS' (blue and red hexagonal lattice), 'MESOPOROUS MATERIALS' (green and yellow porous structure), 'BIOMATERIALS/ BIOELECTRONICS' (yellow and black structure), and 'METAL-ORGANIC FRAMEWORK MATERIALS' (brown and black structure). At the bottom left, the 'AIP | APL Materials' logo is displayed. At the bottom right, a red banner with white text says 'Submit Today!'.

# Downstream plasma transport and metal ionization in a high-powered pulsed-plasma magnetron

Liang Meng,<sup>1</sup> He Yu,<sup>1,2</sup> Matthew M. Szott,<sup>1</sup> Jake T. McLain,<sup>1</sup> and David N. Ruzic<sup>1</sup>

<sup>1</sup>Center for Plasma-Materials Interactions, Department of Nuclear, Plasma, and Radiological Engineering, University of Illinois at Urbana-Champaign, Urbana, Illinois 61801, USA

<sup>2</sup>State Key Laboratory of Electronic Thin Films and Integrated Devices, School of Optoelectronic Information, University of Electronic Science and Technology of China, Chengdu 610054, People's Republic of China

(Received 23 February 2014; accepted 6 May 2014; published online 9 June 2014)

Downstream plasma transport and ionization processes in a high-powered pulsed-plasma magnetron were studied. The temporal evolution and spatial distribution of electron density ( $n_e$ ) and temperature ( $T_e$ ) were characterized with a 3D scanning triple Langmuir probe. Plasma expanded from the racetrack region into the downstream region, where a high  $n_e$  peak was formed some time into the pulse-off period. The expansion speed and directionality towards the substrate increased with a stronger magnetic field ( $B$ ), largely as a consequence of a larger potential drop in the bulk plasma region during a relatively slower sheath formation. The fraction of Cu ions in the deposition flux was measured on the substrate using a gridded energy analyzer. It increased with higher pulse voltage. With increased  $B$  field from 200 to 800 Gauss above racetrack,  $n_e$  increased but the Cu ion fraction decreased from 42% to 16%. A comprehensive model was built, including the diffusion of as-sputtered Cu flux, the Cu ionization in the entire plasma region using the mapped  $n_e$  and  $T_e$  data, and ion extraction efficiency based on the measured plasma potential ( $V_p$ ) distribution. The calculations matched the measurements and indicated the main causes of lower Cu ion fractions in stronger  $B$  fields to be the lower  $T_e$  and inefficient ion extraction in a larger pre-sheath potential. © 2014 AIP Publishing LLC. [<http://dx.doi.org/10.1063/1.4878622>]

## I. INTRODUCTION

High power pulsed magnetron sputtering (HPPMS) has been developed as a new ionized physical vapor deposition (iPVD) technique by applying a high power pulse of low frequency and low duty cycle to the cathode to create a very high plasma density. When high pulse voltage (around 1 kV) is applied to the target, very high peak power density of several kW/cm<sup>2</sup> can be produced. Dense plasmas of  $10^{19}$ – $10^{20}$  m<sup>-3</sup> are generated in front of the target, enhancing the ionization of the sputtered material and producing large ion fluxes. This is generally referred to as high-powered impulse magnetron sputtering (HiPIMS).<sup>1</sup> Great efforts have been made to characterize the HiPIMS plasma and understand the physical mechanisms of HiPIMS discharge, as well reviewed in Refs. 2–5. Langmuir probes of various types are used to study the temporal behaviors of plasma properties such as electron density  $n_e$ , electron temperature  $T_e$ ,<sup>6–9</sup> or more accurately the electron energy distribution functions (EEDF) during pulses.<sup>10,11</sup> Ionization degrees of the sputtered materials have been measured using optical emission spectroscopy (OES), absorption spectroscopy, and mass spectroscopy, etc.<sup>12–15</sup> Generally, HiPIMS plasmas are much more intense and heavily ionized, with drastic variation of EEDF from a broad distribution to eventually Maxwellian-like distribution.<sup>10,16,17</sup> The discharge mechanisms to generate and sustain the intense HiPIMS plasmas are revealed to be very unique, involving the self-sputtering by the ions of the target materials<sup>13,18</sup> in conjunction with gas recycling,<sup>19</sup> gas rarefaction,<sup>20–22</sup> and strong localization of ionization,<sup>23,24</sup> etc. Plasma transport process is also complex and needs

further understanding. So far there have been theories of ion acoustic waves<sup>7</sup> and anomalous transport of electrons across the magnetic field lines with a simultaneous deformation of the magnetic field.<sup>25,26</sup>

The enhanced ionization in HiPIMS can facilitate various metal and compound film deposition and modification processes, such as to achieve an ultra-dense structure and a very smooth surface, to tailor the phase, to modify electrical and optical properties of the films, or to enhance the film adhesion by ion implantation.<sup>3,27–32</sup> HiPIMS may also be found applicable for some processes during integrated circuit (IC) fabrication, for example, the interconnect metallization which requires conformal deposition of metal layers and diffusion barriers in high aspect ratio interconnects.<sup>33</sup> For all of these applications, the process performances will critically rely on the downstream plasma properties, especially near the substrate level. Most studies on HiPIMS mentioned above have been performed or focused on the near-target region. It is thus important to diagnose the plasma in the entire chamber space to understand how plasma transports towards the substrate, to determine the distribution patterns of the plasma over time, and to define which factors affect this process. In HiPIMS, the generated ions are easily recycled for self-sputtering rather than escaping towards the substrate. It is thus desired to measure the fractions of metal ions on the substrate level to directly correlate them to the process performance, and to find methods to promote the ion extraction.

In this study, a triple Langmuir probe (TLP) was used to measure the time-resolved pulsed plasma parameters such as electron density  $n_e$ , electron temperature  $T_e$ , and floating

potential  $V_f$  in a commercial-size magnetron system with a copper (Cu) target. A 3D probe scanning allowed mapping of these parameters in the entire discharge region. The magnetic field strength along with other discharge parameters was varied to reveal the influences on the plasma generation and transport pattern. Meanwhile, the Cu ion fractions in the deposition fluxes were measured using a gridded energy analyzer (GEA) combined with a quartz crystal microbalance (QCM).<sup>34</sup> Theoretical calculations are performed to understand the ion extraction process. In the calculations, the diffusion process of sputtered Cu flux towards the substrate is considered, the mapped  $n_e$  and  $T_e$  data are used to find ionizing probability, the ion extraction efficiency is determined based on the plasma potential ( $V_p$ ) distribution. The possibility of using the magnetic field strength to control the downstream ion flux is also discussed. It should be mentioned that a wide range of peak power densities were used in this study, some of which were below that for typical HiPIMS mode. Therefore, the pulsed discharges in the experiments here were generally referred to as HPPMS instead of HiPIMS.

## II. EXPERIMENTAL SETUP

A large MRC GALAXY planar magnetron system with a 36 cm diameter Cu target was used for this study. The distance between the substrate and the target was kept at 14 cm. The chamber diagram is shown in Fig. 1. A turbo pump was used to achieve a base pressure of  $5 \times 10^{-4}$  Pa. Argon (Ar) gas was supplied, with the working pressure typically kept at 0.67 Pa. A Huettinger TruPlasma Highpulse 4002 DC Generator was used for HPPMS. The plasma generator charges its capacitor to a voltage of 500–2000 V and outputs pulses of 1 to 200  $\mu$ s long. The charging voltage  $V_{ch}$ , the pulse on-time  $t_p$ , and the repetition frequency  $f$  are the basic pulsing parameters. A typical set of discharge parameters were 800 V, 50  $\mu$ s, 100 Hz, 0.67 Pa as the  $V_{ch}$ ,  $t_p$ ,  $f$ , and pressure. The pulse voltage and current were measured on the target using a high voltage probe and a current monitor, respectively.

The magnetron has an adjustable magnet pack behind the target. Simple circular arrangement of the magnets was used in the current study to form a ring-shaped sputtering “racetrack.” By changing the number of magnets used, the

maximum magnetic flux intensity parallel to the target  $B_{//}$  could be varied between 200, 500, and 800 Gauss just above the racetrack as determined using a magnetometer. The three configurations are noted as “200 G,” “500 G,” and “800 G” configurations, respectively.

A simple and well-studied technique to measure the instantaneous  $T_e$  and  $n_e$  without the need of sweeping probe voltages is triple Langmuir probe (TLP),<sup>35</sup> and this has been commonly used in pulsed plasma studies.<sup>7,9,36</sup> It was also adopted in this study for time-resolved diagnostics of the pulsed plasma. Its electrical setup is illustrated in Fig. 1. A fixed bias ( $V_{13}$ ) of about 55 V was applied between probe 1 and 3 with a battery pack to collect the ion saturation currents. Probe 2 was electrically floating in the plasma discharge and measured the floating potential  $V_f$ . All three probe tips are tungsten wires of 0.25 mm in diameter and 8.8 mm in length, separated by 4.0 mm. Such dimensions were chosen to satisfy the collisionless thin sheath criterion and to prevent the interaction between probe tips.<sup>36</sup> Two differential probes were used to measure  $V_{12}$  and the potential drop  $V_{34}$  across a resistor  $R$ . Electron density and temperature can then be calculated using Eqs. (1) and (2). In the present study, the triple probe could be moved in the discharge region radially from  $r=0$  (the central axis) to  $r=14$  cm (near the chamber wall) and axially from  $d=1$  cm (near the target) to  $d=13$  cm (near the substrate). The 3D probe scanning allowed mapping of the plasma distribution in the entire large discharge region.

$$\frac{1}{2} = \frac{1 - \exp\left(-\frac{eV_{12}}{kT_e}\right)}{1 - \exp\left(-\frac{eV_{13}}{kT_e}\right)}, \quad (1)$$

$$\frac{V_{34}}{R} = \exp\left(-\frac{1}{2}\right) A e n_e \sqrt{\frac{kT_e}{M}}. \quad (2)$$

The triple Langmuir probe data have been interpreted with great caution.<sup>37</sup> TLP theory uses an assumption of Maxwellian EEDF. The high-energy electrons typically observed in the early stage of the HPPMS discharge can lead to an over-estimation of the effective electron temperature.

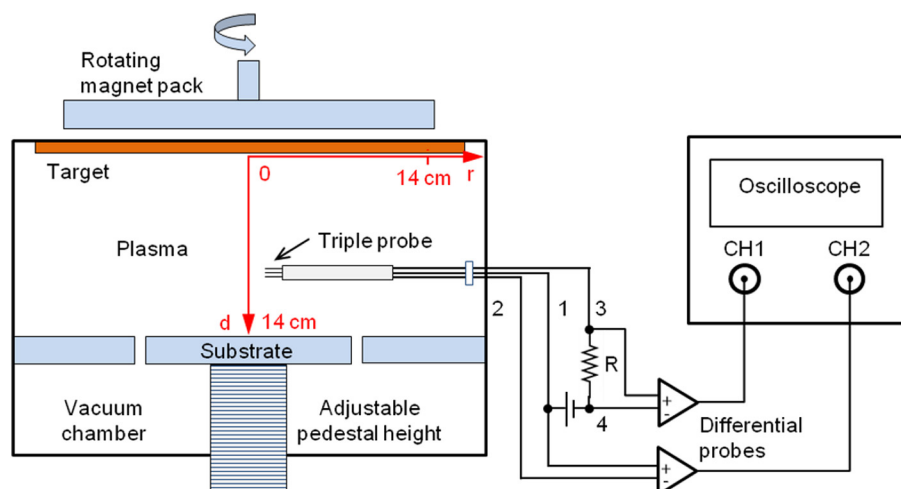


FIG. 1. Schematic diagram of the Galaxy magnetron system with 3D triple Langmuir probe setup. A 36 cm diameter Cu target was used. The triple probe could be moved in radial direction and in axial direction.

However, this has minimum impact on the current study, because the first 20  $\mu\text{s}$  of discharge with foreseeable over-estimation of  $T_e$  is not the main focus. After the first 20  $\mu\text{s}$ , plasma density quickly and substantially increases with strong magnetic confinement. The frequent ionization collisions and Coulomb collisions drive the EEDF to quickly evolve into a Druyvesteyn,<sup>16</sup> bi-Maxwellian,<sup>10</sup> or Maxwellian<sup>17</sup> distribution. As shown in a later section, the determined  $T_e$  is typically lower than 4 eV after the first 20  $\mu\text{s}$  indicating an effective relaxation of the hot electrons and the EEDF becoming close to Maxwellian. More discussions on the concerns of TLP method have been provided in Ref. 37.

To differentiate the fluxes of metal atoms and ions, a GEA combined with a QCM<sup>34</sup> was designed and placed in the downstream plasma. Its schematic is shown in Fig. 2 and the details of the design are described in another paper.<sup>38</sup> The GEA was placed above the QCM and had a ceramic casing with an inner diameter of 30 mm. Three layers of mesh grids were evenly placed inside with a gap of 6.4 mm. The wire distance in the mesh was 0.282 mm with 50% transparency. This distance was smaller than the sheath thickness on the wire to avoid any plasma leak. The top mesh grid was floating to minimize disturbance to the plasma while the middle grid (the electron repeller grid) was negatively biased (typically at around  $-30$  V) to reduce the electron penetration. The bottom grid (the ion repeller grid) was applied a varied voltage from  $-50$  V to  $30$  V to admit or repel ions. Correspondingly, the deposition rate of the total metal flux  $\phi_{tot}$  or that of only metal neutral flux  $\phi_N$  was recorded by the QCM sensor. Gas atoms and ions do not contribute to the deposition rate with the low grid biases adopted. One improvement of the current setup was that the QCM was isolated from ground and could be biased negatively to make sure ions can reach the sensor. Additionally, the metal water cooling tubes were replaced with plastic ones. The ground shielding of the QCM signal coaxial cable was cut open and a capacitor of about  $1 \mu\text{F}$  was added in to complete the path for the high frequency QCM oscillation signal. The metal ion fraction (IF) in the total metal flux can be calculated using Eq. (3), where a geometrical factor  $G$  is included. This originates from the consideration that for the non-directional neutral flux, the ceramic casing will shadow part of the neutrals from reaching the QCM sensor while there is no shadowing effect for directional ion flux. A more specific description on the calculation of  $G$  was done by Green *et al.*<sup>34</sup> For the current GEA setup,  $G = 0.42$  will be used in the calculation assuming an isotropic distribution of neutrals

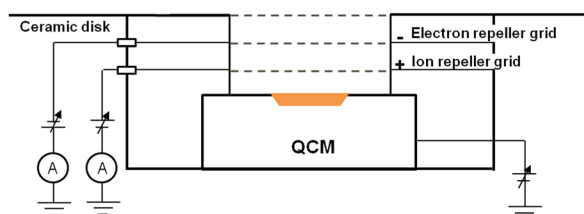


FIG. 2. Schematic of the GEA and QCM assembly. QCM can be floating or biased.

$$IF = \frac{\phi_{tot} - \phi_N}{\phi_{tot} - \phi_N + \phi_N/G}. \quad (3)$$

### III. EXPERIMENTAL RESULTS

#### A. Discharge characteristics

The I-V characteristics of the pulsed discharge were first measured under different discharge conditions and in different magnetic field configurations. Fig. 3(a) shows the I-V waveforms as a function of charging voltage  $V_{ch}$  from 700 to 1000 V. These were measured in the 500 G configuration. Other discharge parameters were  $t_p = 50 \mu\text{s}$ ,  $f = 100$  Hz, and  $p = 0.67$  Pa. The higher  $V_{ch}$  clearly led to higher peak current, which increased from 200 to 650 A. For all charging voltages tested, the pulse voltage on the cathode was seen to drop quickly from the charging voltage to about 330 V. A large voltage might have been induced on the inductors from the impedance matching circuit of the pulsing generator and from the power cable as the current ramped up. The Higher  $V_{ch}$  on the cathode initially provided each secondary electron with a higher energy to generate more electron-ion pairs and build up the plasma faster. Given that the ionization rate is directly proportional to  $n_e$ , a larger current ramping rate was maintained even after the voltage on the cathode dropped to a similar level.

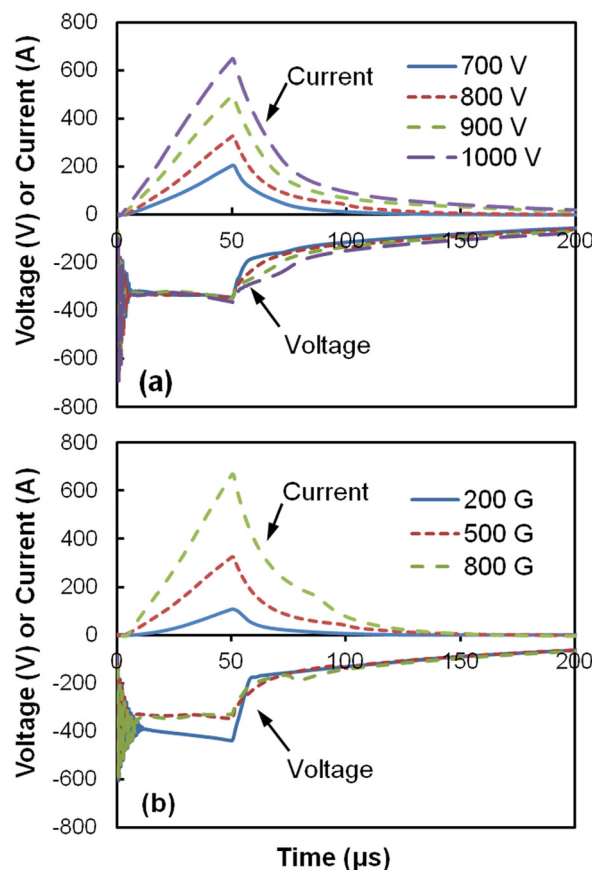


FIG. 3. Discharge I-V characteristics in different conditions and configurations. (a) Typical I-V characteristics for 500 G configuration with varied charging voltage. Recipe was 800–1000 V, 50  $\mu\text{s}$ , 100 Hz, 0.67 Pa. (b) I-V characteristics for 200 G, 500 G, and 800 G configurations. Recipe was 800 V, 50  $\mu\text{s}$ , 100 Hz, 0.67 Pa.



The influences of magnetic field strength on discharge characteristics were then examined. The discharge parameters were kept the same at 800 V, 50  $\mu$ s, 100 Hz, and 0.67 Pa. Fig. 3(b) shows that by increasing  $B_{||}$  on the target surface from 200 to 800 Gauss, higher current was generated. An enhanced electron confinement led to a more intense plasma accumulated near the racetrack. The magnitude of the pulse voltage in stronger B field configuration was lower, since it was easier to maintain the discharge. The peak power density over the entire target in the 800 G configuration reached 240 W/cm<sup>2</sup>. This is much higher than that in DC magnetron sputtering but appears to be lower than the typical power densities of kW/cm<sup>2</sup> in HiPIMS. However, it should be mentioned that only a ring-shaped racetrack was used in order to get the simplest plasma expansion pattern, and the racetrack only covered 1/10 of the whole target area. The power density calculated above is thus somewhat an underestimation if directly compared with the power densities reported in the literature. With this in mind, the discharge in 800 G should be close to HiPIMS mode as defined as to have a peak power density >500 W/cm<sup>2</sup>.<sup>5</sup> For 500 G and 200 G, the peak densities were about 120 and 50 W/cm<sup>2</sup>, respectively, and may not be in the HiPIMS mode even after considering the small racetrack area to target area ratio. But they are still within the peak power density range of more broadly defined HPPMS (>50 W/cm<sup>2</sup>).<sup>5</sup> The peak power densities for some pulsing conditions used in this work are listed in Table I.

## B. Triple Langmuir probe measurement

A triple Langmuir probe was used to measure the time-resolved plasma parameters, including electron temperature  $T_e$  and density  $n_e$ , and their spatial distribution. Measurements were performed in different magnet configurations. Discharge parameters of 800 V, 50  $\mu$ s, 100 Hz, and 0.67 Pa were used. Fig. 4 shows an example of analyzed  $T_e$  and  $n_e$  in the 800 G configuration. Measurements were conducted at different distances  $d$  to the target, right below the racetrack at about  $r = 10$  cm.  $T_e$  was observed to be very high at the beginning until  $t = 25$   $\mu$ s at all locations. This was from a burst of hot electrons accelerated by the applied voltage. There were considerable errors in the  $T_e$  calculation in this period due to the non-Maxwellian distribution, but their overall high values were expected. Then  $T_e$  kept decreasing to several eV during the pulse, while  $n_e$  continued to increase.  $T_e$  were also observed to be lower when closer to the target. Near the target,

TABLE I. The peak power densities with varied charging voltage  $V_{ch}$  in different magnetic field configurations. Other discharge parameters were the same as 100  $\mu$ s pulse duration, 100 Hz, and 0.67 Pa. Note the racetrack area was about 1/10 of the target area.

$V_{ch}$ (V)	Peak power density (W/cm <sup>2</sup> )		
	In 200 G	In 500 G	In 800 G
700	18	70	133
800	51	118	236
900	94	170	308
1000	154	231	390

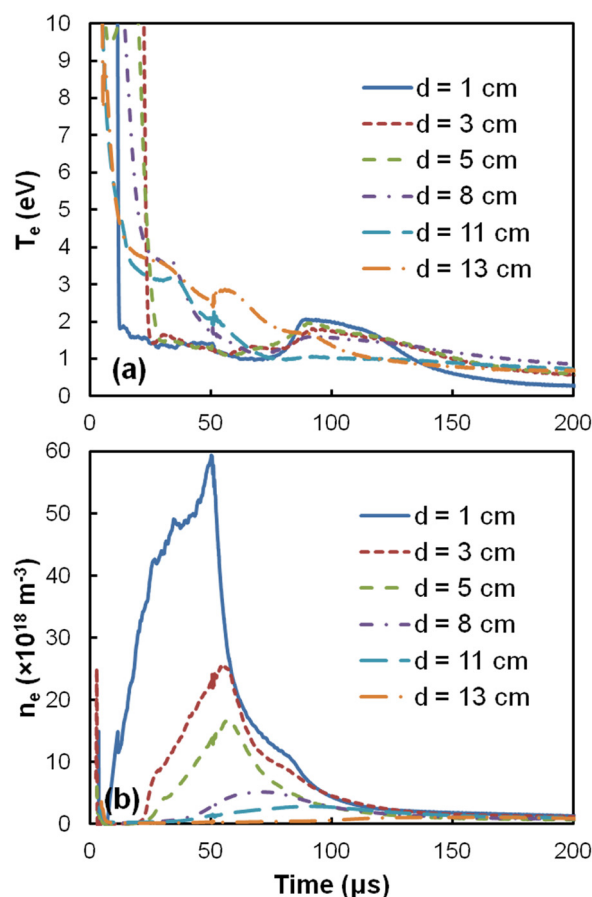


FIG. 4. Temporal behaviors of (a)  $T_e$  and (b)  $n_e$  at different axial distances  $d$  to the target, right below the racetrack at about  $r = 10$  cm. The 800 G configuration was used as an example, while the discharge parameters were 800 V, 50  $\mu$ s, 100 Hz, and 0.67 Pa.

the plasma was strongly confined to build up a higher density, which resulted in more frequent Coulomb collisions. After the pulse ended,  $T_e$  basically continued to decrease.

$T_e$  were also measured in 200 G and 500 G configurations, with some selected data shown in Table II. Similar trends can be seen in these two configurations that  $T_e$  basically decreased with time from the pulse beginning and became higher when moving away from the target racetrack towards the substrate. Some deviations from the trend

TABLE II. The electron temperature  $T_e$  (eV) measured in three magnetic field configurations 200 G, 500 G, and 800 G.  $T_e$  at different distance  $d$  below the racetrack ( $r = 10$  cm) and at selected times from the pulse beginning are shown. The discharge parameters were 800 V, 50  $\mu$ s, 100 Hz, 0.67 Pa.

Configuration	200 G				500 G				800 G			
Time ( $\mu$ s)												
d (cm)	30	50	75	100	30	50	75	100	30	50	75	100
1	2.6	1.8	0.9	0.6	1.7	1.4	1.0	1.4	1.7	1.3	1.0	1.5
3	3.3	1.8	0.9	0.8	1.8	1.1	1.0	1.3	1.7	1.2	1.3	1.7
5	3.2	3.0	0.9	0.8	2.5	1.4	1.1	1.5	1.9	1.3	1.4	1.8
8	2.9	3.6	1.7	1.1	2.6	2.1	1.0	0.8	3.6	1.7	1.2	1.7
11	4.4	4.2	2.1	1.3	2.7	2.1	1.1	0.8	2.9	2.0	1.0	1.1
13	8.4	4.9	2.6	1.7	2.8	2.4	1.3	1.1	3.6	2.6	1.5	1.3

happened with  $T_e$  slightly increasing after the pulse at about  $t = 80 \mu\text{s}$  to form a peak, which can be observed in Fig. 4(a). The cause of this peak still needs further study, but it showed up in both 500 G and 800 G configurations and within 8 cm from the target, not in 200 G configuration or near the substrate. As for the effect of B field strength, it is observed that 200 G configuration produced overall higher  $T_e$  than the stronger magnetic field configurations did, which could be correlated to its lower electron density for less frequent Coulomb collisions. Also its weaker magnetron confinement could not confine high energy electrons effectively and allowed electrons to escape before losing much energy.

As for  $n_e$ , it basically increased during the pulse. When measured near the target, it reached the peak of about  $6.0 \times 10^{19} \text{ m}^{-3}$  at about  $t = 50 \mu\text{s}$ , after which the pulse was off and  $n_e$  quickly reduced. At locations towards the substrate, it was seen that after the pulse was off,  $n_e$  still continued to increase for some time. For example, at  $d = 11 \text{ cm}$ ,  $n_e$  reached its peak of about  $2.8 \times 10^{18} \text{ m}^{-3}$  at  $t = 90 \mu\text{s}$ , much higher than the density at the end of the pulse ( $t = 50 \mu\text{s}$ ). Such an “after-pulse”  $n_e$  peak is believed to originate from

the plasma expansion out of the magnetic confinement region. At different positions, the magnitude and the arrival time of this peak varied. To understand the mechanisms guiding the plasma expansion, a 3D mapping of the plasma expansion peaks was performed.

The after-pulse peak  $n_e$ , and the peak delay time defined as the time interval between the pulse end and the peak arrival time, were measured at different positions, from near the target ( $d = 1 \text{ cm}$ ) to near the substrate ( $d = 13 \text{ cm}$ ), as well as from the chamber center line ( $r = 0$ ) to close to the chamber wall ( $r = 14 \text{ cm}$ ). Fig. 5 shows the mapping of these two parameters in 200 G, 500 G, and 800 G, respectively. In all three cases, peak  $n_e$  was located at about  $r = 10 \text{ cm}$  corresponding to the racetrack ring on the target. With a higher magnetic field strength, the peak power density went up (Table I), and the plasma became denser in the racetrack region. Plasma density quickly decreased as the probe moved away from this region. However, the three configurations showed different expansion patterns. In the 200 G configuration, the expansion was nearly isotropic to produce a relatively uniform plasma distribution near the substrate. In the

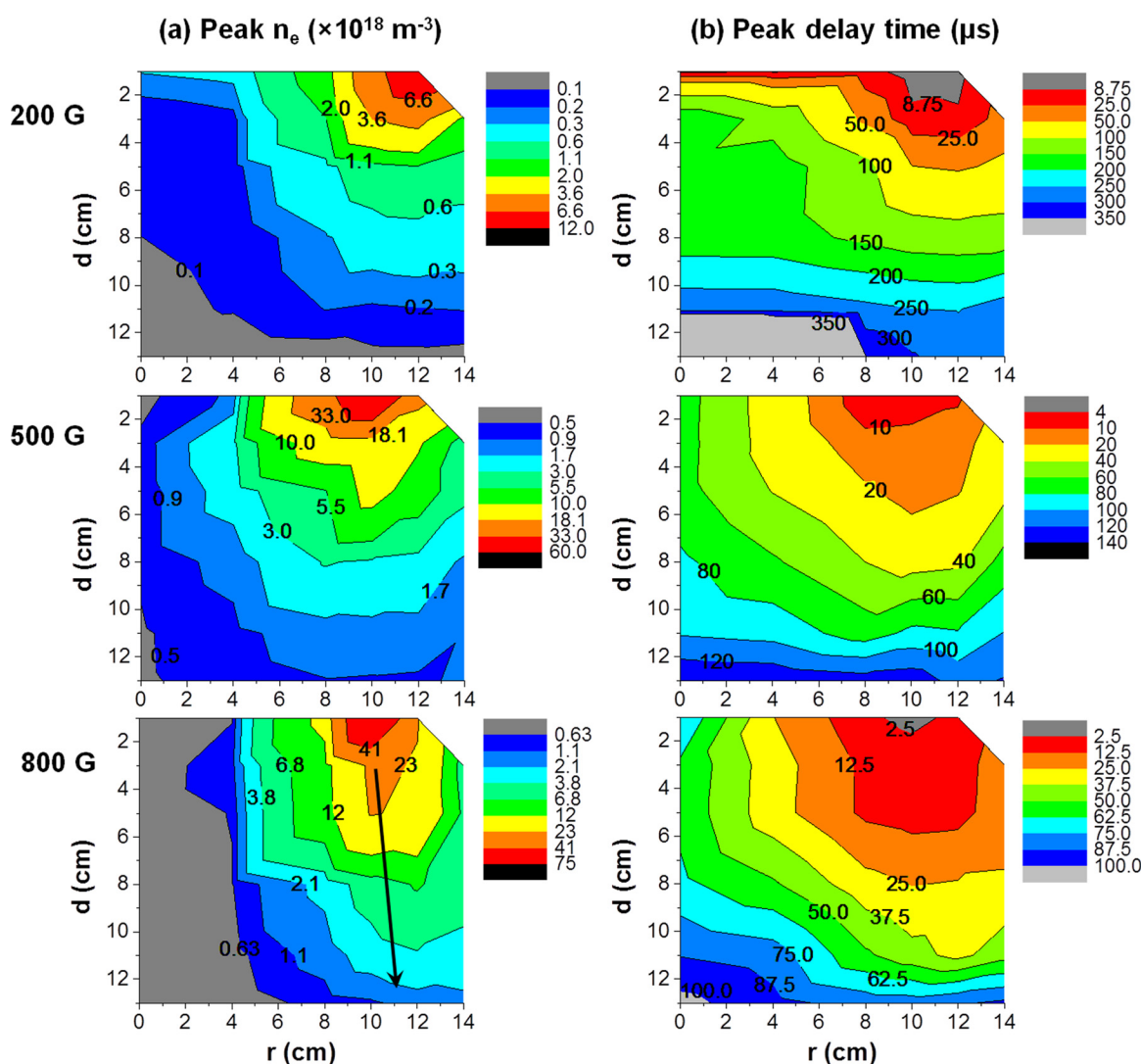


FIG. 5. Peak  $n_e$  after pulse and the corresponding peak delay time vs. various magnetic field strengths (200–800 Gauss), (a) peak density of the expanding plasma, (b) delay time of the expansion peak.

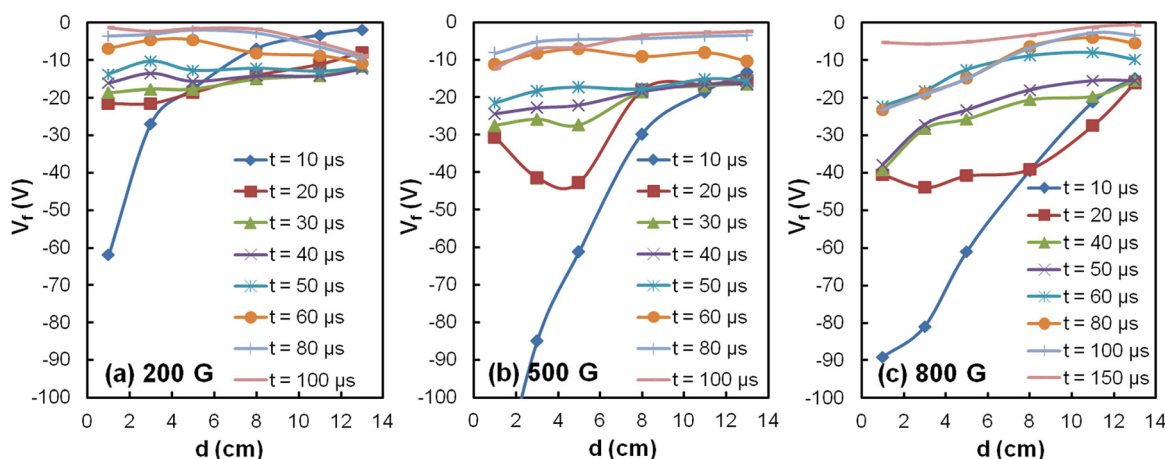


FIG. 6. The evolution of plasma floating potentials  $V_f$  at varied axial positions ( $d$  from 1 to 13 cm,  $r=10$  cm) in (a) 200 G, (b) 500 G, and (c) 800 G configurations.

800 G configuration, the expansion was more directional toward the substrate, leading to very low peak densities along the center axis of the chamber, even lower than those in the 500 G configuration. Comparing the peak delay time in three cases, it can be seen a stronger B field led to a faster expansion, especially in the axial direction. In the 200 G case, the expansion was the slowest but reached different radial positions on the substrate at similar times.

The floating potentials  $V_f$  were also measured in all three magnetic field configurations. Fig. 6 shows the  $V_f$  from  $d=1$  cm to  $d=13$  cm right below the racetrack ( $r=10$  cm) at different times. With plasma potential  $V_p$  approximately tracking with the  $V_f$ , the figures depict the formation of plasma sheath and pre-sheath. At the beginning of the pulse, there was a large potential drop across the entire chamber length between the target and the substrate as a result of the applied pulse voltage. The potential drop in the bulk plasma region gradually decreased and eventually a nearly flat potential was established between  $d=1$  cm and  $d=13$  cm. A high voltage sheath was formed very close to the target analogous to the case of the DC plasma. It took about 30  $\mu$ s for the 200 G configuration to reach this state but a much longer time in the 800 G configuration. The development of sheath involves the re-distribution of charges in plasma, mainly via the drifting of electrons under the electric field force. A delay in achieving flat potential in the bulk plasma region is thus expected in the 800 G configuration, with strong magnetic field confinement to retard the electron drifting and diffusion in the axial direction and to build up a very high  $n_e$  close to the target. It is also noticed that in the 200 G configuration,  $V_f$  decreased towards the substrate after  $t=80$   $\mu$ s, opposite to the trend at the early stage of the pulse. The reason is not completely understood but may be correlated to the slightly higher  $T_e$  near the substrate than that near the target as shown in Table II.  $V_f$  is approximately lower than  $V_p$  by  $4.7T_e$  in Ar plasma.<sup>39</sup> Assuming the plasma potential became equally distributed across the chamber length,  $V_f$  would appear lower near the substrate. The trend was not obvious for the 500 G and 800 G configurations, likely because the  $T_e$  differences were less significant and the plasma potential itself could still be increasing toward the substrate, especially for 800 G case.

### C. Ion fraction measurement

Using the GEA/QCM assembly, ion fractions in the Cu deposition flux were measured on the substrate level. The experiments were performed in 200, 500, and 800 G configurations to study the effect of B field strength. The pulse charging voltage  $V_{ch}$  was also varied. The corresponding peak power density can be seen in Table I.

Fig. 7 shows that the Cu ion fraction basically increased with  $V_{ch}$  in all three B field designs. This was expected, since with higher  $V_{ch}$ , discharge current and peak power were higher and  $n_e$  dramatically increased to facilitate the ionization process. One exception was for voltages higher than 900 V in the 200 G configuration. The  $T_e$  was measured to decrease with higher  $V_{ch}$ , for example, from 1.8 eV at 800 V, to 1.0 eV at 900 V, and to 0.8 eV at 1000 V, all measured at  $d=3$  cm in front of the racetrack at  $t=50$   $\mu$ s. Consequently, the ionization process became less effective. Two factors may have contributed to this  $T_e$  decrease with higher  $V_{ch}$ . The corresponding higher  $n_e$  in the racetrack region led to more frequent Coulomb collisions to reduce the  $T_e$ . Also the voltage on the target increased so that the electrons were accelerated to greater velocities. The weak 200 Gauss

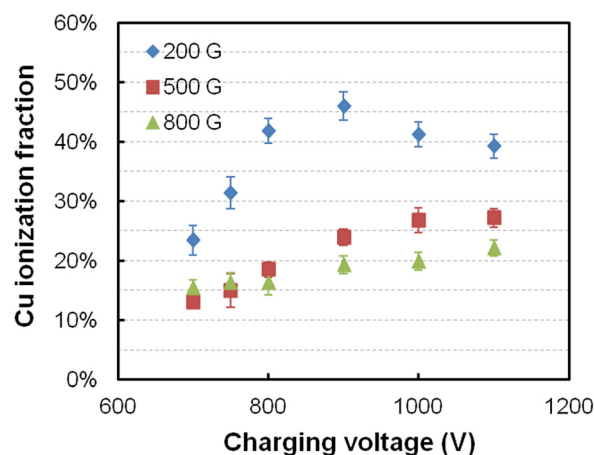


FIG. 7. Ion fractions in the Cu deposition flux were measured on the substrate at different charging voltages. 200, 500, and 800 G configurations were used.



magnetic field became less efficient for the plasma confinement and thus plasma enhancement.

Overall, the 200 G configuration generated the highest Cu ion fraction in the deposition flux, up to about  $46 \pm 2\%$ . For the same discharge recipe with a stronger B field, this fraction was reduced. For example, the Cu ion fractions for pulses of  $V_{ch} = 800$  V were measured to be  $42 \pm 2\%$ ,  $19 \pm 1\%$ , and  $16 \pm 2\%$  for 200, 500, and 800 G configurations. These results seem to contradict the fact that stronger magnetic fields produce much denser plasma. Further discussion will be given in Sec. IV B, considering other factors such as electron temperature, plasma potential distribution. These fractions were lower than the 70% measured by Kouznetsov<sup>1</sup> in a different magnetron system using the method of weight gain. Such a difference still needs some further understanding.

## IV. DISCUSSIONS

### A. On plasma expansion

In Sec. III B, the 3D TLP measurements depicted the plasma transport as expanding from the racetrack to the downstream region. The expansion speed and preferred orientation were seen to depend closely on the magnetic field strength. This phenomenon is further discussed here.

In a magnetron plasma, electrons are confined by the magnetic field via the  $\mathbf{E} \times \mathbf{B}$  drift and the diamagnetic drift. Meanwhile, electrons can still diffuse across the magnetic field, and drift along the electric field if the magnetic field is weak. The diffusion speed is proportional to the diffusion constant perpendicular to magnetic field,  $D_{\perp}$ . In classical diffusion theory, it is known that the diffusion is strongly retarded by the magnetic field.  $D_{\perp}$  is smaller than the diffusion coefficient without a magnetic field,  $D$ , by a factor of  $1 + (\omega_c \tau_m)^2$ , as described in Eq. (4). Here,  $\omega_c$  is the gyration frequency and  $\tau_m \equiv 1/\nu_m$  ( $\nu_m$  is the momentum transfer frequency),  $\bar{r}_c$  is the mean gyroradius which is inversely proportional to B. A higher magnetic field thus has a lower diffusion coefficient, allowing a higher-density plasma to build up. However, once the density is high enough, the Coulomb collisions become very intense with increased  $\nu_m$ , and the diffusion can still be effective. It should be mentioned that non-classical diffusion has been observed in HiPIMS, where the effective collision time for electrons is much shorter and has a weaker dependence on the magnetic field strength.<sup>5,25</sup> This mechanism leads to an enhanced cross-B diffusion but does not explain the faster expansion in a stronger B field configuration

$$D_{\perp} = \frac{D}{1 + (\omega_c \tau_m)^2} = \frac{\pi}{8} \bar{r}_c^2 \nu_m. \quad (4)$$

The electrons diffusing out of the confined plasma region are subjected to drifting in the electric field. As shown in Fig. 6, a larger potential drop and thus, a stronger electric field existed along the axial direction for the time period of interest in the 800 G configuration. The increased drifting toward the substrate therefore prompts a higher expansion speed. On the contrary, the drifting in the 200 G case was

less significant, and the diffusion seems to be the dominant process to result in a more isotropic, but slower, expansion.

### B. On Cu ion fraction

The Cu ion fraction on the substrate was measured to be lower in a stronger magnetic field. To further understand this result, the ionization probability needs to be calculated, which not only depends on  $n_e$  but is also strongly affected by the electron temperature  $T_e$ . It should also be kept in mind that the generated ions may be re-directed to the target instead of being extracted towards the substrate if a large electric field is present.<sup>40</sup>

Herein, a theoretical model is built to quantitatively predict the fraction based on the measured plasma parameters. A number of assumptions are made to simplify the model. (1) The collision/diffusion of the neutral fluxes is one-dimensional. It is assumed the Cu atoms sputtered out of the target have 2 eV (Ref. 39) and are only in the axial direction instead of following a cosine angle distribution. The flux is slowed down by collisions between Cu atoms and cold Ar atoms, with a cross-section  $\sigma_{M,Ar}$  based on a hard-sphere model. The mean free path for Cu atoms is then  $\lambda_{Cu,Ar} = 1/(n_{Ar} \sigma_{M,Ar})$ . Here,  $n_{Ar}$  is the atom density of Ar gas. Each collision reduces the velocity of Cu atoms based on the Cu to Ar mass ratio. The velocity of the Cu atom flux at different positions as well as the time delay getting to that position can then be determined, as shown in Table III. The arrival time delay is about 100  $\mu$ s to reach the substrate. (2) The ionization is assumed to be induced by electron impact ionization only. The Penning ionization and charge exchange collisions are neglected, which is a reasonable assumption based on the statements by Raadu *et al.*<sup>41</sup> The Cu ionization rates  $K_{iz}$  are calculated based on the cross-section data taken from Ref. 42.  $P_{iz}$ , the probability of a Cu atom being ionized per unit distance (in this case 1 cm) at different locations can then be determined via Eq. (5)

$$P_{iz} = 1 - \exp(-n_e K_{iz} / v_M). \quad (5)$$

Here,  $v_M$  is the local velocity of Cu atom flux. The Cu ions created in each segment will be redirected to the target if the local electric field is large. Practically about 2 V/cm was chosen as the criterion with considerations of the initial ion energy being retained from the sputtered Cu atoms, the time needed for ions to slow down, and time-varying plasma potential distribution. Specific analyses were done for the initial stage of the pulse because of fast and dramatic plasma potential variation. Again, floating potentials are used here since they basically track with the plasma potential.

TABLE III. The calculated velocities of the sputtered Cu atom flux to arrive at different axial positions  $d$  from the target and the corresponding time delays.

$d$ from target (cm)	1	3	5	8	11	13
Velocity of Cu atom flux (m/s)	2495	2054	1691	1263	943	776
Arrival time delay ( $\mu$ s)	3.8	12.7	23.4	44.0	71.6	95.0



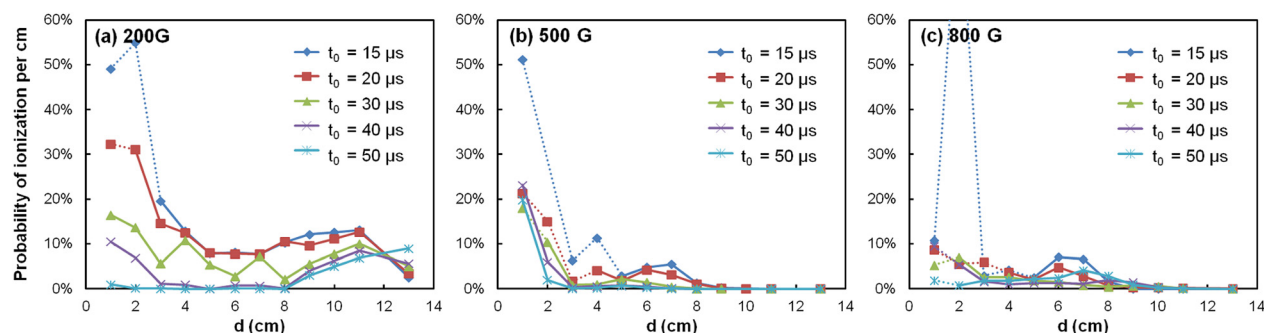


FIG. 8. Probability of Cu atoms being ionized per cm. Calculations were done for different axial distances  $d$  from the racetrack, time of Cu atoms being sputtered out ( $t_0$ ), and B field configurations (a) 200 G, (b) 500 G, and (c) 800 G. The ions generated at certain positions marked as the dotted segments are predicted to be re-directed towards the target, while those in the solid segments are to be extracted towards the substrate.

With these assumptions, the Cu atom fluxes from the target generated at different times ( $t_0$ ) were calculated using the pulse voltage, pulse current, and Ar<sup>+</sup>-Cu sputtering yield data. Based on the arrival time of the flux, the ionization probabilities  $P_{iz}$  were determined using the measured  $T_e$  and  $n_e$  data. These probabilities are plotted in Fig. 8 for all three B field strengths. The ionization for flux generated in the first 15  $\mu$ s was not included because the measured  $T_e$  might not be accurate, and the sputtered flux was low enough to be safely neglected. The dotted line implies that the plasma potential drop prevents the ion extraction there. Several points should be noted. (1)  $P_{iz}$  is usually high near the target largely because of the high  $n_e$  there. (2) Flux generated earlier is usually more highly ionized. This is because of high  $T_e$  during the initial stage of the pulse. (3) There is still some substantial ionization at later times in the range from the midpoint to the substrate. Recall that the electron density is sustained at the downstream locations by the plasma expansion, so that even the Cu neutral flux arriving after a delay time as long as 100  $\mu$ s (Table III) can still be ionized to a certain degree. (4) Finally, the 200 G configuration shows the highest  $P_{iz}$  overall, mainly because it has higher  $T_e$  (e.g., 1.8–4.9 eV at  $t=50 \mu$ s, as shown in Table II) than the other configurations and the plasma potential flattens very quickly allowing for more efficient ion extraction. On the other hand, 800 G has very high plasma density and the magnetic confinement region is larger. This not only lowers the  $T_e$  (e.g., about 1.3–2.6 eV at  $t=50 \mu$ s) due to frequent Coulomb collisions but also leads to a larger and wider pre-sheath (Fig. 6) which inhibits the ion extraction.

All of the ion fluxes that can be extracted (indicated by solid lines) are then added up and compared with the remaining Cu neutral flux to get the ion fraction on the substrate. It should be noted that various factors can contribute to an error of the estimation. These factors include limited spatial resolution for the triple probe measurements, errors of the measured  $T_e$  and  $n_e$ , the simplified method of using local electric potentials to determine the ion extraction, and treating the diffusion in one dimension instead three dimension in the entire chamber. As a result, the model results are expected to have about 20% of error. For 200 G, 500 G, and 800 G, the predicted Cu ion fractions are then  $51 \pm 10\%$ ,  $25 \pm 5\%$ , and  $15 \pm 3\%$ , respectively, which match the measured values of

$42 \pm 2\%$ ,  $19 \pm 1\%$ , and  $16 \pm 2\%$  within the margin of error. In other words, the simplified model was able to explain the ionization results by determining the ionization probability and the ion extraction efficiency. It should be mentioned that a more accurate estimation of Cu ion fractions requires a more sophisticated model and better spatial resolution for the  $T_e$  and  $n_e$  measurement.

## V. CONCLUSIONS

Downstream plasma transport in a high-powered pulsed-plasma magnetron system was studied using 3D triple Langmuir probe measurements. Plasma expansion was observed with a high plasma density peak moving from the target racetrack region towards the substrate. With an increased magnetic field strength from 200 Gauss to 800 Gauss, a much denser plasma was generated, which expanded faster with more directionality towards the substrate as opposed to nearly isotropic expansion in the 200 Gauss configuration. The sheath formation took a longer time in an 800 Gauss field, resulting in a pre-sheath with larger potential drop extending into the bulk plasma region. The corresponding electric field promoted the electron drift and increased the expansion velocity and directionality. The magnetic field strength is thus an important parameter to consider for controlling the downstream plasma distribution.

Cu ion fractions were measured on the substrate level. Up to  $46 \pm 2\%$  was achieved using a 200 Gauss magnetic field configuration, much higher than the DC magnetron sputtering. It basically increased with higher charging voltage, but decreased with a stronger B field despite a much higher plasma density. A comprehensive model was built to explain this observation. It was shown that the ion fraction on the substrate level was determined not only by the electron density but also by the electron temperature to affect the ionization probability, the transport of the sputtered Cu atoms, and the ion extraction efficiency dictated by the plasma potential gradient. The main causes of lower Cu ion fractions in stronger B field were the overall lower  $T_e$  and inefficient ion extraction due to the larger pre-sheath potential drop. A properly controlled low magnetic field confinement, however, may help optimize the metal ion fractions on the substrate level for process improvement.

## ACKNOWLEDGMENTS

This study was supported by the Center for Lasers and Plasma in Advanced Manufacturing (National Science Foundation, Grant No. CMMI09-53057). The authors would like to gratefully acknowledge Dexter Magnetic Technologies for providing the adjustable magnetron pack and Huettinger Electronic for providing the pulsed plasma generator.

- <sup>1</sup>V. Kouznetsov, K. Macák, J. M. Schneider, U. Helmersson, and I. Petrov, *Surf. Coat. Technol.* **122**, 290 (1999).
- <sup>2</sup>U. Helmersson, M. Lattemann, J. Bohlmark, A. P. Ehiasarian, and J. T. Gudmundsson, *Thin Solid Films* **513**, 1 (2006).
- <sup>3</sup>J. Alami, S. Bolz, and K. Sarakinos, *J. Alloys Compd.* **483**, 530 (2009).
- <sup>4</sup>K. Sarakinos, J. Alami, and S. Konstantinidis, *Surf. Coat. Technol.* **204**, 1661 (2010).
- <sup>5</sup>J. T. Gudmundsson, N. Brenning, D. Lundin, and U. Helmersson, *J. Vac. Sci. Technol. A* **30**, 030801 (2012).
- <sup>6</sup>J. W. Bradley, H. Bäcker, P. J. Kelly, and R. D. Arnell, *Surf. Coat. Technol.* **135**, 221 (2001).
- <sup>7</sup>J. Alami, J. T. Gudmundsson, J. Bohlmark, J. Birch, and U. Helmersson, *Plasma Sources Sci. Technol.* **14**, 525 (2005).
- <sup>8</sup>Th. Welzel, Th. Dunger, H. Kupfer, and F. Richter, *J. Appl. Phys.* **96**, 6994 (2004).
- <sup>9</sup>P. M. Bryant, S. A. Voronin, J. W. Bradley, and A. Vetushka, *J. Appl. Phys.* **102**, 043302 (2007).
- <sup>10</sup>J. T. Gudmundsson, J. Alami, and U. Helmersson, *Surf. Coat. Technol.* **161**, 249 (2002).
- <sup>11</sup>J. T. Gudmundsson, P. Sigurjonsson, P. Larsson, D. Lundin, and U. Helmersson, *J. Appl. Phys.* **105**, 123302 (2009).
- <sup>12</sup>A. P. Ehiasarian, R. New, W.-D. Münz, L. Hultman, U. Helmersson, and V. Kouznetsov, *Vacuum* **65**, 147 (2002).
- <sup>13</sup>S. Konstantinidis, J. P. Dauchot, M. Ganciu, A. Ricard, and M. Hecq, *J. Appl. Phys.* **99**, 013307 (2006).
- <sup>14</sup>J. Bohlmark, M. Lattemann, J. T. Gudmundsson, A. P. Ehiasarian, Y. A. Gonzalvo, N. Brenning, and U. Helmersson, *Thin Solid Films* **515**, 1522 (2006).
- <sup>15</sup>J. Vlcek, P. Kudlacek, K. Burcalova, and J. Musil, *Europhys. Lett.* **77**, 45002 (2007).
- <sup>16</sup>A. D. Pajdarova, J. Vlcek, P. Kudlacek, and J. Lukas, *Plasma Sources Sci. Technol.* **18**, 025008 (2009).
- <sup>17</sup>S.-H. Seo, J.-H. In, and H.-Y. Chang, *Plasma Sources Sci. Technol.* **14**, 576 (2005).
- <sup>18</sup>A. Anders, J. Andersson, and A. P. Ehiasarian, *J. Appl. Phys.* **102**, 113303 (2007).
- <sup>19</sup>A. Anders, J. Capek, M. Hala, and L. Martinu, *J. Phys. D: Appl. Phys.* **45**, 012003 (2012).
- <sup>20</sup>S. M. Rossnagel and H. R. Kaufman, *J. Vac. Sci. Technol. A* **6**, 223 (1988).
- <sup>21</sup>J. Vlcek, A. D. Pajdarova, and J. Musil, *Contrib. Plasma Phys.* **44**, 426 (2004).
- <sup>22</sup>J. Alami, K. Sarakinos, G. Mark, and M. Wuttig, *Appl. Phys. Lett.* **89**, 154104 (2006).
- <sup>23</sup>A. Anders, *Appl. Phys. Lett.* **100**, 224104 (2012).
- <sup>24</sup>A. Anders, P. Ni, and A. Rauch, *J. Appl. Phys.* **111**, 053304 (2012).
- <sup>25</sup>J. Bohlmark, U. Helmersson, M. VanZeeland, I. Axnäs, J. Alami, and N. Brenning, *Plasma Sources Sci. Technol.* **13**, 654 (2004).
- <sup>26</sup>D. Lundin, P. Larsson, E. Wallin, M. Lattemann, N. Brenning, and U. Helmersson, *Plasma Sources Sci. Technol.* **17**, 035021 (2008).
- <sup>27</sup>J. Alami, P. O. Å. Persson, J. Bohlmark, J. T. Gudmundsson, D. Music, and U. Helmersson, *J. Vac. Sci. Technol. A* **23**, 278 (2005).
- <sup>28</sup>K. Sarakinos, J. Alami, and M. Wuttig, *J. Phys. D: Appl. Phys.* **40**, 2108 (2007).
- <sup>29</sup>S. Konstantinidis, J. P. Dauchot, and M. Hecq, *Thin Solid Films* **515**, 1182 (2006).
- <sup>30</sup>J. Alami, P. Eklund, J. M. Andersson, M. Lattemann, E. Wallin, J. Bohlmark, P. Persson, and U. Helmersson, *Thin Solid Films* **515**, 3434 (2007).
- <sup>31</sup>M. Lattemann, A. P. Ehiasarian, J. Bohlmark, P. Å. O. Persson, and U. Helmersson, *Surf. Coat. Technol.* **200**, 6495 (2006).
- <sup>32</sup>A. P. Ehiasarian, J. G. Wen, and I. Petrov, *J. Appl. Phys.* **101**, 054301 (2007).
- <sup>33</sup>A. Dulkan, E. Ko, L. Wu, I. Karim, K. Leaser, K. J. Park, L. Meng, and D. N. Ruzic, *J. Vac. Sci. Technol. A* **29**, 041514 (2011).
- <sup>34</sup>K. M. Green, D. B. Hayden, D. R. Julianio, and D. N. Ruzic, *Rev. Sci. Instrum.* **68**, 4555 (1997).
- <sup>35</sup>S. Chen and T. Sekiguchi, *J. Appl. Phys.* **36**, 2363 (1965).
- <sup>36</sup>L. Meng, A. N. Cloud, S. Jung, and D. N. Ruzic, *J. Vac. Sci. Technol. A* **29**, 011024 (2011).
- <sup>37</sup>H. Yu, L. Meng, M. Szott, J. T. Meister, T. S. Cho, and D. N. Ruzic, *Plasma Sources Sci. Technol.* **22**, 045012 (2013).
- <sup>38</sup>L. Meng, R. Raju, R. Flauta, H. Shin, D. N. Ruzic, and D. B. Hayden, *J. Vac. Sci. Technol. A* **28**, 112 (2010).
- <sup>39</sup>M. A. Lieberman and A. J. Lichtenberg, *Principles of Plasma Discharge and Materials Processing* (Wiley, New York, 1994).
- <sup>40</sup>J. Capek, M. Hala, O. Zabeida, J. E. Klemberg-Sapieha, and L. Martinu, *J. Phys. D: Appl. Phys.* **46**, 205205 (2013).
- <sup>41</sup>M. A. Raadu, I. Axnäs, J. T. Gudmundsson, C. Huo, and N. Brenning, *Plasma Sources Sci. Technol.* **20**, 065007 (2011).
- <sup>42</sup>R. S. Freund, R. C. Wetzell, R. J. Shul, and T. R. Hayes, *Phys. Rev. A* **41**, 3575 (1990).